Vadose Zone Journal Accepted Paper, posted 02/14/2013 doi:10.2136/vzj2012.0147

Monitoring Vadose Zone Desiccation with Geophysical Methods

M.J. Truex[1,*], T.C. Johnson[1], C.E. Strickland[1], J.E. Peterson[2], and S.S. Hubbard[2]

Submitted: October 2, 2012
Accepted: January 31, 2013
Vadose Zone Journal

[*]Corresponding Author
[1]Energy and Environment Directorate
Pacific Northwest National Laboratory
P.O. Box 999, MS K6-96
Richland, WA 99354
mj.truex@pnl.gov
509-371-7072

[2]Lawrence Berkeley National Laboratory
1 Cyclotron Road, MS 90-1116
Berkeley, CA 94720

Abstract

Soil desiccation was recently field tested as a potential vadose zone remediation technology. Desiccation removes water from the vadose zone and significantly decreases the aqueous-phase permeability of the desiccated zone, thereby decreasing movement of moisture and contaminants. The 2-D and 3-D distribution of moisture content reduction over time provides valuable information for desiccation operations and for determining when treatment goals have been reached. This type of information can be obtained through use of geophysical methods. Neutron moisture logging, cross-hole electrical resistivity tomography, and cross-hole ground penetrating radar approaches were evaluated with respect to their ability to provide effective spatial and temporal monitoring of desiccation during a treatability study conducted in the vadose zone of the DOE Hanford Site in WA.

Introduction

In situ remediation is a potential approach to address contaminants located in the vadose zone at depths below the limit of direct exposure where remediation is focused on protection of groundwater (Dresel et al. 2011). Although a vast body of research has been performed to investigate in-situ remediation of groundwater systems, significantly fewer studies have been dedicated to remediation of contaminated vadose zone regions. Concurrent with development of remediation approaches, successful vadose zone remediation will also require effective methods of remedy performance monitoring. In 2008, the Department of Energy (DOE) initiated a treatability test program to evaluate the potential of several deep vadose zone remedies for protection of groundwater (DOE 2008) with assessment of approaches that mitigate the transport of inorganic and radionuclide contaminants from the vadose zone to the groundwater. Soil desiccation was investigated as a potential vadose zone remediation technology, including laboratory studies (Ward et al. 2008; Oostrom et al. 2009, 2012a,b; Truex et al. 2011), modeling studies (Ward et al. 2008; Truex et al. 2011), and field testing (Truex et al. 2012a, b) conducted as part of the treatability test efforts at the DOE Hanford Site.

Desiccation of a portion of the vadose zone, in conjunction with a surface infiltration barrier, has the potential of minimizing migration of deep vadose zone contaminants towards the water table (Truex et al. 2011). To apply desiccation, a dry gas is injected into the subsurface. The dry gas evaporates water from the porous medium until the gas reaches 100% relative humidity and can no longer evaporate water. Evaporation can remove pore water and result in very low moisture content in the desiccated zone (Ward et al. 2008; Oostrom et al. 2009; Truex et al. 2011). The desiccation process removes previously disposed and native water from the vadose zone and significantly decreases the water relative permeability of the desiccated zone. Due to

these desiccation-induced changes, the future rate of movement of moisture and contaminants through this zone is decreased.

The performance of desiccation in terms of mitigating future moisture movement is related to the extent of moisture content reduction and the location and thickness of the desiccated zone (Truex et al. 2011, 2012a, b). Reducing the moisture content below the residual moisture content value for the sediment is a target for desiccation because the of the low resulting water relative permeability (Truex et al. 2012a, b). Information about the distribution of moisture content reduction over time is needed for performance monitoring during desiccation implementation. These data are important for determining when desiccation has met treatment goals and thus when the process can be stopped. Monitoring data can also be used to guide operational decisions, such as adjustments in system flow rates and injection gas properties. While nominal values for these injection parameters can be selected based on initial site characterization data, the impact of subsurface heterogeneities cannot be fully predicted. As such, monitoring is needed to assess the impact of these heterogeneities on desiccation performance. The objective of this study was to evaluate the effectiveness of technologies for monitoring desiccation under field conditions. Several geophysical approaches were tested for monitoring desiccation-induced changes in moisture and temperature at the Hanford Site desiccation field test, including neutron moisture logging, temperature logging, cross-hole ground-penetrating radar and cross-hole electrical resistivity tomography.

Geophysical methods have been used extensively in the last decade to characterize and monitor subsurface hydrological processes (e.g., Rubin and Hubbard, 2005; Vereecken et al., 2006). Because geophysical data can be collected from many different platforms (e.g., from satellites and aircraft, at the ground surface of the earth, and at or between wellbores), the geophysical

data can provide remote subsurface characterization or monitoring information over a variety of spatial scales and resolutions. The main advantage of using geophysical data over conventional measurements is that geophysical methods can provide spatially extensive information about the subsurface in a minimally invasive manner at a comparatively high resolution. The greatest disadvantage is that the geophysical methods only provide indirect proxy information about subsurface hydrological properties or processes.

Soil moisture content determination in the vicinity of a wellbore using neutron scattering probes has become a standard method over the past several decades (Hignett and Evett 2002). A neutron probe consists of a high energy neutron source, a low energy or thermal neutron detector, and the electronics required for counting and storing the measured response. A fast neutron source manually placed within moist soil develops a dense cloud of thermal neutrons around it and a thermal neutron detector placed near the source samples the density of the generated cloud. The concentration of thermalized neutrons is affected by both soil density and elemental composition. Elements that absorb neutrons are often in low concentration in the soil solid phase and when clay content is also low, the neutron probe response is mainly affected by changes in moisture content (Greacen et al. 1981; Hignett and Evett 2002). Neutron moisture logging data can typically be collected with high vertical resolution and can be converted to volumetric moisture content (VMC) using published or site-specific relationships. Interpolation of neutron moisture logging data between multiple measurement wellbores can be used to generate an estimated 2-D or 3-D moisture content distribution.

Ground Penetrating Radar (GPR) methods are also commonly used to characterize or monitor subsurface moisture content. GPR methods use electromagnetic energy at frequencies of ~10 MHz to 1GHz to probe the subsurface. At these frequencies, the dielectric polarization

within a material that has been subjected to an external electric field dominates the electrical response. GPR systems consist of an impulse generator which repeatedly sends a particular voltage and frequency signal to a transmitting antenna. Cross-hole GPR methods involve lowering a transmitter into a wellbore and measuring the vertical electric field with a receiving antenna that is lowered down another wellbore. The transmitting and receiving antennas are manually relocated to different positions in the wellbores to facilitate transmission of the energy through a large fraction of the area between the measurement boreholes.

Together, the electrical properties of the host material and the frequency of the GPR signal primarily control the sampling volume and the depth of penetration of the signal. The electromagnetic velocity (V) is dependent on the permittivity (ε), conductivity (σ), frequency (ω) and magnetic permittivity (μ, assumed to be equal to free space) of the subsurface material through which the signal travels as:

$$V = \left\{ \frac{\mu\varepsilon}{2} \left[\sqrt{1+\left(\frac{\sigma'}{\omega\varepsilon} \right)^2} + 1 \right] \right\}^{-\frac{1}{2}} \qquad (1)$$

The loss tangent is a useful metric for determining low-loss conditions and is defined as the electrical conductivity divided by the product of the dielectric permittivity and the angular frequency. In general, GPR performs better in low-loss environments, such as unsaturated coarse or moderately coarse textured soils. GPR signal strength is strongly attenuated in electrically conductive environments (such as systems dominated by the presence of clays or high ionic strength pore fluids). When low-loss conditions prevail, the velocity depends primarily on the permittivity, which can be expressed as (Davis and Annan, 1989):

$$\varepsilon \approx \left(\frac{c}{V}\right)^2, \quad (2)$$

where c is the propagation velocity of electromagnetic waves in free space. The velocity of the GPR signal can be obtained by measuring the travel time of the signal over a known distance between the transmitter and the receiver. Using measurements acquired from antennae located at many different vertical positions within each borehole and inversion algorithms, a 2-D image of GPR velocity between boreholes can be produced through tomographic inversion (e.g., Jackson and Tweeton 1994; Peterson, 2001) and used with (2) to estimate the 2-D permittivity distribution.

Soil dielectric permittivity is strongly dependent on moisture content because of the large difference between water and bulk soil permittivity. The relative permittivity (the dielectric permittivity of a material divided by the free space permittivity, ε_0) of water is approximately 80, compared to values between 3 and 7 for typical soil mineral components. As such, under low-loss and unsaturated conditions, GPR velocity is primarily influenced by moisture variability and secondarily by texture, although texture can influence moisture dynamics and thus the effective GPR response (Grote et al., 2010). Studies have demonstrated that GPR methods can effectively estimate and monitor subsurface moisture content using measured electromagnetic velocities (Hubbard et. al. 1997; Van Overmeeren et al. 1997; Huisman et al. 2001; Binley et.al 2002; Day-Lewis et al. 2002; Laloy et al. 2012). The dielectric permittivity of soils and sediments also depends on temperature (Or and Wraith, 1999). However, for this paper we considered temperature effects to be negligible based on laboratory core permittivity measurements made over the temperature range of this experiment, which corresponded to estimated VMC errors of less than $0.01 m^3/m^3$ (data not shown).

Several different petrophysical relationships have been used to translate permittivity into moisture content estimates (Huisman et al., 2001). An example is shown in Equation 3, where volumetric moisture content, θ, is a linear function of the square root of the soil apparent dielectric permittivity, ε_a (Ledieu et al. 1986; White et al. 1995; Topp and Ferré 2002):

$$\theta = A\sqrt{\varepsilon_a} + B, \quad (3)$$

where A and B are fitted parameters. In this study, we use the coefficients determined by Topp and Reynolds (1998) of A = 0.115 and B = -0.176. The term apparent is used here to mean the dielectric permittivity value that is inferred from measurement of the velocity of an electromagnetic wave at a given frequency. In this study, water content values obtained using Equation 3 deviated from those derived using the polynomial Topp's equation (Topp et al, 1980; Topp and Ferré 2002) by less than $0.01 m^3 m^{-3}$. General guidelines for GPR acquisition, processing and water content estimation are provided by Annan (2005) and Huisman et al (2001).

Electrical Resistivity Tomography (ERT) is a method of remotely imaging the electrical conductivity (C) of the subsurface that has been commonly used to monitor subsurface moisture variations (e.g., Binley and Kemna, 2005; Revil et al. 2012). For cross-hole ERT applications, electrodes installed within boreholes are used to strategically inject currents and measure the resulting potentials to produce a data set that is used to reconstruct the subsurface C structure (Daily and Owen, 1991; Johnson et al., 2010). In unsaturated sediments, C can be influenced by clay content, granulometric properties, salinity, and temperature (Lesmes and Friedman, 2005) , although moisture content (Slater and Lesmes, 2002) often dominates the response. Thus, temporal changes in moisture content during desiccation can be monitored by imaging

corresponding changes in C using ERT. General guidelines associated with ERT acquisition, inversion, and interpretation are provided by Binley and Kemna (2005).

In granular materials with a non-conductive solid phase, the bulk C can be described according to (Revil et al., 2012),

$$C = \sigma_f \emptyset^m S_w^n + \emptyset^m S_w^{n-1} \beta_{(+)} \bar{Q}_V \quad (4)$$

where σ_f is the fluid conductivity, ϕ is the porosity, S_w, is the water saturation, m is the cementation exponent, and n is the water saturation exponent. $\beta_{(+)}$ represents the mobility of the cations in the pore water, and $\bar{Q}_V$ is the charge per unit pore volume of the diffuse part of the electrical double layer. The first term of Equation 4 describes the component of C arising from ionic current flow within the pore water (Archie, 1942). The second term of Equation 4 describes the component of C arising from current flow along the pore-grain interface within the electrical double layer; the so-called surface conductivity. In clean, low-clay sands with relatively small surface area, C is dominated by the first term in Equation 4. The Hanford Formation, where our experiment was conducted, is comprised of high energy flood deposits, consisting of coarse gravels and sands with interbedded fine sands and silt-sized materials (Serne et al. 2009). We assume, therefore, that the second term of Equation 4 is insignificant, and consider only the first term of Equation 4 (e.g. Archie's Law). Although we have no direct information supporting the validity of Archie's Law, as will be subsequently demonstrated, the comparison between changes in water content derived from C using Archie's Law and actual changes in water content measured by neutron probe are favorable, suggesting that our assumption is reasonable. In addition to the Archie's Law assumption, the relationship between temporal changes in water

saturation and the corresponding changes in C that occur during subsurface desiccation can be simplified under the following assumptions:

1) ϕ and *m* are constant in time. These parameters are dependent on the textural properties of the sediment and this assumption may be appropriate for many sites.

2) σ_f is constant in time. This assumption is not strictly valid because ionic concentrations increase as pore water is evaporated during desiccation, but may be appropriate for many sites. This assumption was validated with core-scale measurements in this case (data not shown), and also with comparison neutron probe measurements of changes in water content.

3) *n* is independent of saturation. This assumption may be appropriate for many sites, although at low water saturation values (< ~ 5%) *n* has been observed to decrease with decreasing water saturation (Waxman and Smits, 1968; Han et. al. 2009; Hamamoto et al. 2010).

If the assumptions stated above are valid, a desiccation-induced change in water saturation can be derived from Equation 4 in terms of the corresponding change in bulk C as

$$\frac{S_t}{S_0} = 10^{\frac{1}{n} log_{10}\left(\frac{C_t}{C_0}\right)} \qquad (5)$$

where S_t is the water saturation at time *t*, S_0 is the pre-desiccation baseline water saturation, and C_t and C_0 are the corresponding bulk conductivity at time *t* and pre-desiccation. As we will show, errors arising from the assumptions leading to Equation 5 exist, but are not so large as to invalidate ERT derived changes in saturation expressed through the saturation ratio. It is important to note that the same assumptions may not fare as well at other sites. Note also that the

ratios of VMC and water saturation are equivalent. Because desiccation is a non-isothermal process, the effects of temperature on bulk conductivity must also be considered. The temperature dependence of bulk conductivity in the vadose zone is dependent on moisture content, but is always monotonic (Waxman and Thomas, 1974).

Temperature sensors can also provide a means to monitor the progress and distribution of desiccation using a network of in situ sensors. Temperature decreases due to evaporative cooling until the desiccation front reaches the monitoring locations (i.e., the time when the sediment between the injection location and the monitoring location is desiccated). At that time, the temperature at the monitoring location begins to increase toward the temperature of the injected gas because evaporative cooling is no longer occurring in the sediment between the injection location and the monitoring location (Oostrom et al. 2009). There can be multiple inflection points if there are multiple layers that are being desiccated at different rates and these layers are within a region that can impact the temperature at the monitoring location.

This paper presents an assessment of selected geophysical monitoring approaches applied before and during the desiccation field test at the Hanford Site. The methods were evaluated with respect to their ability to provide effective spatial and temporal monitoring of desiccation. Benefits and limitations of the methods were considered based on the characteristics of the data collection and analysis techniques.

Geophysical Monitoring of Field Desiccation Experiment

Field Test Summary

The desiccation field test was conducted in the vadose zone at the U.S. DOE Hanford Site 200-BC-1 Operable Unit as described by Truex et al. (2012a, b) and summarized below. The total

198 thickness of the vadose zone beneath the 200-BC-1 Operable Unit is about 100 m. About 110
199 million liters of aqueous waste containing high concentrations of solutes was disposed at
200 multiple engineered cribs and trenches, primarily in the 1950s. Figure 1 shows the pre-
201 desiccation characterization data for vertical stratigraphy, electrical conductivity (corresponding
202 to the contaminant distribution), and moisture distribution at the test site injection and extraction
203 wells in relation to the well screen interval. The test was conducted within the Hanford
204 Formation and porous media grain-size variations in the test interval range from sand to loamy
205 sand (which is similar to the porous media observed throughout the full depth interval). The
206 injection well is located between adjacent waste disposal cribs where the subsurface was
207 impacted by lateral movement of crib discharges.

208 A dipole configuration was used for the field test with injection of dry nitrogen gas and
209 extraction of soil gas through wells screened in a target depth interval from 9.1 to 15.2 m below
210 ground surface (bgs) to favor soil gas flow within this interval and within a defined monitoring
211 zone. The general operational and in situ monitoring strategy is depicted in Figure 2. Use of dry
212 nitrogen gas at a controlled temperature of 20^{o}C provided a constant inlet condition with a
213 relative humidity of zero. Injection occurred at a stable flow rate of 510 m^3/h from January 17,
214 2011 through June 30, 2011 (164 days) except during a 13-day interval from April 21 through
215 May 4, 2011 when there was no injection. Extraction of soil gas was maintained for the full test
216 duration at a stable flow rate of 170 m^3/h. The injection and extraction wells were 12-m apart.
217 Figure 3 depicts the lateral layout of injection and extraction wells and the monitoring locations.
218 A 30 m by 45 m gas-impermeable membrane barrier was installed at the surface centered over
219 the well network to inhibit soil gas flow at the ground surface.

A clustered monitoring approach was used in the test whereby a sensor borehole, containing sensors for temperature and ERT electrodes, was placed nominally adjacent to a cased, unscreened logging well used to conduct manual neutron moisture logging and to acquire cross-hole GPR data. Sensor boreholes (21.3 m total depth) were constructed with alternating 0.76-m-thick zones of 100-mesh (> 0.125 and < 0.149 mm) Colorado sand (Colorado Silica, Colorado Springs, CO) and granular bentonite from 3 to 21.3 m bgs. ERT electrodes were placed within the bentonite zones (e.g., every 1.5 m) with tubing installed to enable addition of water around each electrode to locally hydrate the bentonite and maintain effective coupling between the electrode and the subsurface. Electrical connectivity was checked periodically during the test and water added when necessary to improve electrical coupling where a threshold of >10 mA injected current was used to indicate suitable electrode coupling. Sensor boreholes also contained thermistors every 0.6 m from 3 to 21.3 m bgs. Logging wells extended to 21.3 m bgs with a 2-inch PVC casing (plugged at the bottom) in a 4-inch diameter borehole and 100-mesh Colorado sand in the annular space.

Neutron Moisture Logging

Neutron moisture logging was conducted using a CPN 503DR Hydroprobe (InstroTek Inc., Raleigh, NC). Neutron probe measurements were acquired at depth increments of approximately 7.5 cm using a count time of 30 s and then converted to count ratio (C_R) by dividing each measurement by the standard count.

Neutron probe data were converted to VMC using a site specific relationship described by Truex et al. (2012a) and summarized below. Sediment samples were collected laterally within 0.9 m of the neutron logging well L2 (6 to18 m bgs) after the active desiccation phase of the test and sediment texture ranged from medium sand to loamy sand with the exception of one sample

of sandy silt. Although clay content can also affect moisture content calibration (Greacen et al. 1981), the clay content was low at the desiccation field site, ranging between 2.4% and 8%.

Samples were grouped into sand and loamy sand texture materials. Neutron moisture probe C_R data were plotted with corresponding post-desiccation laboratory-measured VMC (computed using measured gravimetric moisture content and bulk density) from samples at the same depth. Using only samples above 0.05 m^3 m^{-3}, a linear calibration relationship was observed for both sand and loamy sand. Post-desiccation VMC for some of the very dry core samples within the highly desiccated zones (loamy sand and sand textures) were 0.004 +/- 0.002 m^3 m^{-3} from laboratory gravimetric analyses, with corresponding count ratios of 0.21 +/- 0.007. For the loamy sand, using the linear relationship based on only samples above 0.05 m^3 m^{-3} would predict a count ratio of 0.34 for a moisture content of 0.004 m^3 m^{-3}, substantially different from the actual observations. Linear relationships over the full range of data could be applied but provide a poor fit to the data. For this study, a non-linear neutron probe calibration relationship captures the response for both soil types and provides a better fit to the data over the full range (Figure 4). Regression of VMC (θ) and C_R data for all core samples resulted in the relationship $\theta = 0.714C_R^2 - 0.1363C_R$, with a root mean square error of 0.015 for θ and a coefficient of determination of 0.93.

VMC values from pre-desiccation and post-desiccation neutron logging events were interpolated to a finely spaced grid encompassing the logging wells using a weighted inverse-distance interpolation scheme. Due to the high vertical resolution of the data along the logging wells, the corresponding low lateral resolution, and the expected high lateral correlation in moisture content, we chose a 5 to 1 horizontal to vertical weighting in the interpolation. This interpolation provides a smoothed 3-D estimate of VMC distribution.

Ground Penetrating Radar

GPR data were collected with a PulseEKKO 100 using 100 MHz borehole antennas (Sensors and Software, Inc. Missasauga, ON, Canada). Multiple offset gather surveys (Peterson, 2001) were periodically collected between logging well pairs using a vertical offset increment of 0.25 m and an angular coverage of approximately 40 degrees above and below the midpoint of each gather. Wellbore deviation logs were applied to more accurately determine the antenna positions used in the surveys. Borehole pair separation was roughly 3 m and the primary transect was along the plane between the injection and extraction wells (Figure 3). The first arrival times of the energy were picked from the data, and were inverted using MIGRATOM, a curved ray inversion software (Jackson and Tweeton 1994), to yield 2-D electromagnetic velocity estimates along key transects. The data were inverted with no vertical to horizontal anisotropy and using global minimum and maximum velocity constraints of 0 and 0.25 m/ns respectively. The results from each of the inversions produced travel time residual errors less than 1.9 ns. The velocity estimates were converted to dielectric permittivity using Equation 2 (i.e., by assuming low-loss conditions). Equation 3 was used to convert GPR-derived permittivity to VMC content.

At the desiccation site, the C ranges up to 0.330 S/m and the low-loss assumption underlying Equation 2 is not valid at all locations. Low-loss conditions are valid when the loss-tangent is much less than one. For instance, assuming a dielectric permittivity of 10 and a frequency of 100 MHz, the loss tangent will be less than one for C values less than 0.05 S/m. Prior to desiccation, ERT-derived C were less than 0.05 S/m at depths shallower than 10 m. A comparison of baseline near-borehole VMC estimates from GPR (derived using Equations 2 and 3) to those obtained from neutron moisture logging indicate a good correlation for depths less than 10 m where C is less than 0.05 S/m. This comparison is shown in Figure 5 for borehole

L3 and was similar for the other boreholes at the desiccation test site. At depths greater than 10 m, the C was higher than the low-loss assumption cutoff and the linear relationship between VMC estimated from neutron moisture logging and GPR was degraded. Interpretation of GPR data for conditions with higher conductivity will be impacted by violation of the low-loss assumption which can change during the desiccation process as discussed in the next section.

Electrical Resistivity Tomography

ERT data were collected prior to and during desiccation using 99 electrodes; 11 electrodes equally spaced from 6.25 m to 21.5 m deep in each of the 9 sensor wells. Measurements were collected using an 8-channel MPT DAS-1 impedance tomography system (www.mpt3d.com). Full forward and reciprocal measurements were collected twice per day in order to estimate data noise and quality, and each data set contained 6114 measurements after filtering. The data were collected and inverted in 3-D with isotropic (i.e. equal weighting in all directions) first order spatial derivative smoothing constraints on an unstructured tetrahedral mesh with 354,544 elements. The parallel ERT inversion software described by Johnson et al. (2010) was used to invert each data set with 100 processors on parallel computing resources housed at the Pacific Northwest National Laboratory. Elements were refined around electrodes and within the imaging region in order to optimize simulation accuracy and available resolution. Each data set was individually inverted (i.e. no constraints were applied in the time-dimension) and Equation 5 was used to compute the saturation ratio for each element at each ERT survey time.

Core-scale testing on site sediments showed the C response to be primarily governed by decreases in water saturation as opposed to increases in fluid conductivity during desiccation, validating the assumption that fluid conductivity (σ_f) may be considered constant in time (data not shown). In addition, laboratory testing on site sediments showed *n* to be ~2.0 within the

saturation range indicated by neutron moisture logging data during the desiccation test and a constant value of 2.0 was used in Equation 5. The ERT images were also corrected for temperature prior to applying Equation 5. Laboratory testing on Hanford site sediments showed a temperature dependence of 0.00017 S/mC° at 5% VMC and 0.00023 S/mC° at 12% VMC, consistent with published values (Friedman et al. 2005; Ruijin et al. 2010). A constant value of 0.00020 S/mC° was assumed for the temperature dependence and used to correct all C results to a temperature of 20 C° based on the interpolated temperature field.

In order for a sequence of time-lapse ERT inversions to be comparable, each inverted data set must contain the same survey configuration and the same number of measurements. This requirement is problematic when data quality degrades over the course of the monitoring period. At the desiccation site, electrodes were installed within a plug of bentonite in order to facilitate electrical coupling with the host material. Some electrodes within the desiccation zone became poorly coupled to host material upon drying, likely due to bentonite shrinkage and cracking. Measurements using these electrodes had to be removed from every survey in the entire data set in order to produce a consistent set of measurements for the time lapse inversion. This resulted in a loss of sensitivity and image resolution at depth. Figure 6 shows the squared sensitivity of the ERT measurements to the bulk conductivity distribution pre-desiccation (left) and post-desiccation (right), along a 2-D transect intersecting the injection and extraction wells. The post-desiccation decrease in sensitivity in the lower section and below the injection well is caused by the loss of electrodes during desiccation, resulting in an inability to resolve changes below about 15 m depth. This is important when interpreting the forthcoming time-lapse inversion images, which do not indicate the decreases in conductivity below 15 m that are indicated by neutron

logging and radar. Note that this problem can be addressed in future applications by encasing the electrodes in a material less prone to desiccation cracking such as Portland cement grout.

Temperature Monitoring

Thermistors (USP8242 encapsulated negative temperature coefficient thermistors, U.S. Sensor, Orange, California) were used to monitor temperature. To achieve accurate temperature measurements over the range of interest, a fifth-order polynomial was used to relate resistance to temperature for each of the thermistors used in the field test. The manufacturer's calibration relationship was verified for a subset of the thermistors in a precision water bath spanning the 0°C–40°C temperature range with measured accuracies better than 0.07°C.

Temperatures were logged continuously (10 minute intervals) at each thermistor. In addition to use for correcting the ERT-derived C to a standard temperature prior to using the ERT data for estimating VMC changes, 3-D interpolation of the temperature data were also used to evaluate desiccation progress. The 3-D temperature field was estimated at selected times using the same interpolation technique that was used for the neutron moisture data.

Results and Discussion

Neutron moisture logging provides a large number of vertically-discrete data points at multiple lateral locations over time. These data are expected to provide the most accurate and high resolution information about vertical variations in moisture at the borehole locations. Cross-hole ERT and cross-hole GPR are expected to provide indirect but more spatially extensive estimates of moisture content and associated changes over time. The ERT was collected autonomously over several boreholes and thus offers temporally dense information in 3-D; the GPR was collected manually and offers high 2-D spatial resolution but low temporal resolution. The

temperature sensors provided a large number of vertically-discrete data points at multiple lateral locations across the test zone and for multiple time points. In this section, we describe the datasets and their associated interpretations in terms of monitoring the distribution of moisture content reduction over time to at or below a specified threshold moisture content value. We subsequently compare the different data suites and discuss their relative benefits and limitations for monitoring a desiccation treatment zone.

Field Test Data

Neutron moisture logging data over time show changes in VMC at monitored locations that varied with depth and the initial moisture content associated with the sediment texture (e.g., Figure 7). Neutron logging data is expected to be an accurate localized indicator of VMC because of its calibration to physical measurement of moisture content from sediment samples. Desiccation was not uniform across the injection screen depth interval. At each monitoring location, the neutron data show the vertical distribution of desiccation and zones desiccated to below selected threshold moisture content values can be identified. For instance at location L2, the depth interval between about 13 and 17 m bgs was desiccated to a VMC below 0.02 $m^3\ m^{-3}$ by the end of active desiccation. The 3-D distribution of desiccation can be estimated by interpolating the neutron moisture logging data between monitoring locations. Figure 8 shows VMC for a 2-D plane within the 3-D neutron moisture data interpolation. The distribution of moisture content over time can be used to identify where desiccation has reached a specified threshold moisture content, nominally in the 13-17 m bgs depth interval out to a radial distance of about 3 m from the injection well for a threshold of moisture content of 0.02 $m^3\ m^{-3}$ (red zone) by the end of active desiccation in the field test. Interpretation of the 2-D moisture content

representation should consider that interpolation does not incorporate subsurface conditions that can impact the distribution of desiccation away from the measurement point.

The 2-D distribution of desiccation between access wells can also be estimated by cross-hole GPR. Figure 9 shows VMC over time for a series of 2-D GPR surveys between adjacent logging wells (Figure 3). This figure was created using Equations 2 and 3, recognizing that the validity of the low-loss assumption associated with Equation 2 varies both spatially and temporally. Similar to the neutron moisture data, this estimate for the distribution of moisture content over time shows desiccation in the 13-17 m bgs depth interval out to a radial distance of about 3 m from the injection well for a threshold of moisture content of 0.02 m^3 m^{-3} (dark red zone) by the end of active desiccation in the field test. Interpretation of the 2-D moisture content representation should consider that conversion of GPR-derived permittivity to VMC is impacted by C. However, desiccation reduces the C, which renders GPR data acquisition more favorable, and improves the accuracy of the GPR-derived moisture content estimate. For example, Figure 10 shows the ERT-derived C distribution along the GPR survey transect prior to the start of the test (left) and at day 140 of desiccation (right). The black regions illustrate where low-loss assumptions may not be valid (C > 0.05 S/m). Prior to desiccation, the low-loss assumption is generally valid above a depth of 10 m and invalid below10 m. At the end of desiccation, low-conductivity conditions have been established within a zone from depths of approximately 13 m to 15 m. Within this depth interval, GPR derived moisture content estimates correlate well with estimates from neutron moisture logging (Figure 11). Thus, within zones where desiccation has decreased the C, GPR can be used with confidence to estimate the moisture content distribution between wells. At other locations, the estimates should be considered with caution.

The progression and distribution of moisture content changes as imaged by ERT is shown in Figure 12. The ERT data show changes in the VMC expressed as the ratio of VMC at the time of the measurement (VMC_t) to the baseline VMC from an ERT data set collected prior to desiccation (VMC_0), estimated as described in Equation 5 and with recognition that the ratios of VMC and water saturation are equivalent. Thus, a VMC_t/VMC_0 ratio of one designates areas that have not changed from the conditions prior to active desiccation. Ratios lower than one indicate desiccation, for instance, where a ratio of 0.5 means that the VMC is 0.5 times what it was prior to desiccation. The representations shown in Figure 12 are for a 2-D plane extracted from 3-D ERT images. Areas where the VMC_t/VMC_0 ratio becomes less than a specified value (e.g., 0.5) could be used to interpret the distribution of desiccation below a threshold of change (moisture content decreased by half), or below an absolute threshold if used in conjunction with knowledge of the starting moisture content. The resolution of the ERT data inversion is on the order of a cubic meter. Thus, the ERT images in Figure 12 do not resolve sharp contrasts in drying zones over time, but show a "smoothed" image of how the subsurface is changing. Note that changes below approximately 15 m were not resolved by the ERT due to electrode loss as discussed previously.

Figure 13 shows temperature distribution for a 2-D plane extracted from 3-D interpolation of temperature sensor data during active desiccation. These data representations can be used to interpret the distribution of desiccation and obtaining "significant" desiccation based on the distribution of evaporative cooling and post-cooling temperature increases. The progression of cooled zones shown at days 14, 30, and 70 are indicators of desiccation activity (evaporative cooling) and the related dominant injected dry gas flow pattern. By days 140 and 164, localized warming indicates that some zones have been desiccated. Desiccation, as indicated by cooler

423 temperatures, continues to occur at other locations at these times. Interpretation of the 2-D
424 temperature representations should consider that interpolation may not accurately reflect the
425 temperature distribution away from the measurement point.

426 *Comparative Assessment*

427 The geophysical methods and temperature monitoring applied in the field test utilize
428 substantially different methods to provide data for estimating the distribution and extent of
429 moisture content changes during desiccation. For each method, there are benefits and limitations
430 for use of these data to monitor desiccation based on the characteristics of the data collection,
431 analysis techniques, and sources of error. These benefits and limitations also have implications
432 for application of desiccation treatment on a larger scale than was applied for the field test.

433 Neutron moisture logging and GPR data can be converted using calibration approaches to
434 provide VMC locally at a wellbore or within a 2-D plane, respectively. ERT cannot be directly
435 converted to VMC, but changes in ERT-measured C can be converted to corresponding changes
436 in VMC. Temperature monitoring cannot be related to VMC, but is an indicator of desiccation
437 based on evaporative cooling phenomena. Datasets also have different sources of error;
438 examples here include the errors expected based on the low-loss assumption used for the GPR
439 interpretation and the errors associated with the loss of electrode coupling on the ERT
440 interpretation. Thus, each data set needs to be interpreted differently and carefully with respect to
441 monitoring the distribution of desiccation and targeted threshold moisture content.

442 Neutron moisture logging of a borehole is a standard method for obtaining a high resolution
443 vertical profile (~7.5 cm vertical intervals) of VMC that is accurate locally (~30 cm radius) with
444 calibration to sediment data. Temporal resolution of the data depends on manual survey

445 frequency, which may lead to lower temporal resolution than for methods that can operate
446 autonomously. Subsurface conditions would be expected to change most rapidly near a dry gas
447 injection well with responses becoming much slower with larger radial distances. Thus, the need
448 for frequent data associated with reaching desiccation targets is related to the scale of the
449 targeted treatment zone. However, for desiccation operational decisions, more frequent early-
450 term data may be needed to help guide operational adjustments that may impact overall long-
451 term performance.

452 Interpolation of VMC from neutron moisture logging data can be used to generate a three-
453 dimensional image of moisture conditions that may be most appropriate for sites with significant
454 anisotropy leading to dominantly horizontal soil gas flow. However, as the monitoring scale
455 becomes larger, neutron data may become sparse compared to the targeted desiccation volume,
456 depending on the number of access locations installed. For instance, if drying has occurred at
457 one location, but not yet at another location, interpolation cannot effectively project the extent of
458 drying past the first location. As distances between monitoring locations grow larger, larger
459 portions of the subsurface are essentially not monitored for a period of time by neutron data.

460 Cross-hole GPR provides means to monitor VMC in two dimensions based on propagation of
461 energy through the subsurface between two logging boreholes. Thus, it provides data for
462 interpretation of VMC distribution away from subsurface access points and does not require
463 interpolation between access points like the neutron moisture logging data. GPR provides high
464 resolution within the survey plane due to high vertical density of data from multiple offset
465 surveys at the access locations. GPR borehole spacing is constrained by energy propagation and
466 generally needs to be less than 10 m for the vadose zone and even smaller for areas with high C
467 (about 3 m at the desiccation test site). As with the neutron logging data, temporal resolution of

the data depends on manual survey frequency. High C at contaminated sites (e.g., due to high ionic contaminant concentrations in pore water such as present in the lower portion of the test site) can severely impact the accuracy of the GPR estimate. When the ground has a high C the low-loss assumption is not valid and the EM velocity is affected by both C and permittivity changes such that accurate conversion to VMC is difficult. However, in zones with significant desiccation, the C drops because moisture content decreases. In those zones, the low-loss assumption may be valid and GPR data can be used to estimate moisture content through Equations 2 and 3. At the field site, even very high initial conductivity dropped to levels appropriate for the low-loss assumption in desiccated zones.

Cross-hole ERT provides means to monitor the change in VMC in three dimensions based on the imaged C distribution in the subsurface between multiple electrodes. Decreases in temperature and moisture content occur during desiccation, both of which cause a decrease in C. Thus, to improve the accuracy of quantitative estimates of the moisture content change using ERT, a temperature correction is necessary. This correction is moisture content dependent, but in practice, a constant temperature correction factor is applied in the data inversion. In addition, increasing fluid conductivity with decreasing moisture content may dampen the ERT response and impact moisture content change estimates. ERT data provided limited resolution such that the distribution of spatial moisture content change is depicted with lower contrast than actually exists, appearing as a smoothed or blurred representation of actual changes. This issue is applicable with any geophysical method requiring an inversion, such as GPR; however, GPR generally provides higher spatial resolution than ERT given the same access points for electrodes and antennas. With ERT, spatial resolution can be adapted by modifying the electrode distribution and proximity to the desiccation zone, and can be selected to be appropriate for the

scale of the desiccation target and the resolution needed based on the monitoring goals. As shown in Figures 6 and 12, ERT imaging resolution can change over time if electrodes have to be dropped from the network because of electrical coupling issues as the porous medium is desiccated. In the field test, maintaining electrical coupling was difficult in heavily desiccated zones, likely due to bentonite contraction and subsequent separation from electrodes. Full-scale applications would need to consider improved wetting capability or nonshrinkable grout around electrodes to maintain adequate coupling (e.g., neat Portland cement).

A significant benefit of the ERT method is that the data can be collected autonomously, which can greatly improve temporal resolution over manually-collected datasets. Thus, ERT provides the potential for relatively automated imaging of desiccation progress. ERT derived changes in bulk conductivity provide qualitative information concerning when and where desiccation is occurring without interpretation. However, to be quantitative, ERT images must be interpreted to relate the ERT-derived change in VMC (e.g., VMC_t/VMC_0) at the available data resolution to the site-specific metrics for desiccation distribution and threshold moisture content targets. Potentially, using pre-desiccation measurements of initial VMC, a threshold VMC change ratio for reducing the VMC to below a specified threshold could be set (e.g., if the target VMC is 0.02 and the initial VMC is about 0.06, a target change ratio would be about 0.3). Interpretation would need to consider that the ERT data represent average changes within the resolution control volume (e.g., for the field test a volume of about a cubic meter). Final VMC values may need to be confirmed at selected locations with another method like neutron logging or GPR. For the field test, with consideration of the ERT resolution issues at the bottom of the test zone, a VMC reduction of about 50% from the initial moisture content value corresponded to zones where other data also indicated significant desiccation.

Due to the evaporative cooling effect of desiccation, temperature data over time can also be used to interpret desiccation distribution and roughly indicate achieving a threshold of significant desiccation based on inflection of cooling to warming trends. Resolution for these determinations depend on sensor spacing and interpolation of the data are required with related issues as discussed for the neutron logging data. Temperature sensors are robust, relatively inexpensive and data can be collected autonomously. Thus, temperature monitoring appears to be useful as part of a desiccation monitoring approach.

Conclusions

Monitoring the progression of in situ remedies such as desiccation is needed to provide information to guide operational decisions. Additionally, monitoring data are needed to determine when performance requirements such as the size of the desiccated zone and the final moisture content have been met. However, monitoring options for in situ vadose zone remedies are limited and implementation can be challenging due to the subsurface properties and limited access. Geophysical monitoring methods were evaluated as part of a field-scale treatability test of desiccation at the Hanford site with an emphasis on providing spatial and temporal information about the distribution of desiccation and the extent of moisture content reduction. The study also highlighted the benefits and limitations of different borehole and cross-hole methods for monitoring desiccation. Although the method evaluation objective of the study was met, future efforts using joint or coupled inversion approaches and more sophisticated petrophysical relationships (Ferre et al., 2009; Hubbard and Linde, 2011; Laloy et al. 2012) are expected to take advantage of the benefits and compensate for some of the method-specific limitations.

Traditional moisture content monitoring through neutron moisture logging is well established and provides detailed vertical profile information at discrete logging locations. Interpolation of multiple logging locations is possible, but must be applied with caution because interpolation does not account for subsurface heterogeneities away from the logging locations and becomes less representative as the distance between logging locations increases. While GPR moisture content estimates are impacted by high C, estimates in low conductivity and significantly desiccated zones appear to be similar to neutron moisture data. GPR scaling to larger applications may be limited by the need for relatively closely spaced logging access. ERT data can be collected autonomously for good temporal resolution and can provide estimates of moisture content change in three dimensions, but not estimates of absolute moisture content. However, ERT implementation is readily scalable to larger sites. Interestingly, interpolation of temperature data, due to the evaporative cooling effect of desiccation, also provided useful 3-D information about the progress of desiccation and is a robust method for vadose zone implementation.

Acknowledgements

Primary funding for this research was provided by CH2M Hill Plateau Remediation Company, Richland, WA. Additional funding related to refinement of data analysis techniques and conducting ground penetrating radar surveys was provided by the U.S. Department of Energy Office of Groundwater and Soil Remediation and Richland Operations Office as part of the Deep Vadose Zone Applied Field Research Initiative. Pacific Northwest National Laboratory is operated by the Battelle Memorial Institute for the Department of Energy (DOE) under Contract DE-AC06-76RLO 1830. Visualization software was provided by Lawrence Livermore National Laboratory using VisIt. Neutron moisture logging was conducted by the S.M. Stoller

559 Corporation, Hanford Office, under contract to CH2M Hill Plateau Remediation Company,
560 Richland, WA.

561

562 **References**

563 Archie, G.E. 1942. The electrical resistivity log as an aid in determining some reservoir
564 characteristics. Petroleum Transactions of AIME 146:54–62.

565 Annan, P. 2005. GPR methods for hydrogeological studies. In: Rubin Y. and Hubbard S.S. (eds),
566 *Hydrogeophysics*,. Ser. 50, *Springer*, Dordrecht, pp. 185-214.

567 Binley, A., and A. Kemna. 2005. DC resistivity and induced polarization methods. In: Y. Rubin
568 and S. Hubbard, editors, Hydrogeophysics. Springer, The Netherlands. p. 129–156..

569 Binley, A., G. Cassiani, R. Middleton, and P. Winship. 2002. Vadose zone model
570 parameterisation using cross-borehole radar and resistivity imaging. J. Hydrol.
571 267(3–4):147–159.

572 Daily, W., and E. Owen. 1991. Cross-borehole resistivity tomography. Geophysics
573 56:1228–1235.

574 Davis, J.L., and A.P. Annan. 1989. Ground penetrating radar for high resolution mapping of soil
575 and rock stratigraphy. Geophys. Prospect. 37 (5), 531–551.

576 Day-Lewis, F.D., J.M. Harris, and S.M. Gorelick. 2002. Time-lapse inversion of crosswell radar
577 data. Geophysics 67:1740–1752.

578 DOE. 2008. Deep vadose zone treatability test plan for the Hanford Central Plateau.
579 DOE/RL-2007-56, Rev. 0, U.S. Department of Energy Richland Operations Office, Richland,
580 WA.

581 DOE. 2010. Characterization of the soil desiccation pilot test site. DOE/RL-2009-119, Rev. 0,
582 U.S. Department of Energy Richland Office, Richland, Washington.

583 Dresel, P.E., D.M. Wellman, K.J. Cantrell, and M.J. Truex. 2011. Review: Technical and policy
584 challenges in deep vadose zone remediation of metals and radionuclides. Environ. Sci. Technol.
585 45(10):4207–4216.

586 Ferré, T., L. Bentley, A. Binley, N. Linde, A. Kemna, K. Singha, K. Holliger, J. A. Huisman, and
587 B. Minsley. 2009. Critical steps for the continuing advancement of hydrogeophysics. Eos Trans.
588 AGU. 90(23):200, doi:10.1029/2009EO230004.

589 Friedman, S.P. 2005. Soil properties influencing apparent electrical conductivity: A review.
590 Comp. and Elec. in Ag. 46:47–50.

591 Greacen, E.L., R.L. Correll, R.B. Cunningham, O.C. Johns, and K.D. Nichols. 1981. Calibration.
592 In: Soil water assessment by the neutron method. CSIRO, Melbourne, Australia, p. 50–78.

593 Grote, K., C. Anger, B. Kelly, S. Hubbard, and Y. Rubin. 2010. Characterization of soil water
594 content variability and soil texture using GPR groundwave techniques. J. Environmental and
595 Engineering Geophysics. 15(3):93–110.

596 Hamamoto, S., P. Moldup, K. Kawamoto, and T. Komatsu. 2010. Excluded-volume expansion of
597 Archie's Law for gas and solute diffusivities and electrical and thermal conductivities in variably
598 saturated porous media. Water Resour. Res. 46, doi:10.1029/2099WR00842r.

599 Han, M., S. Youssef, E. Rosenberg, M. Fleury, and P. Levitz. 2009. Deviation from Archie's
600 Law in partially saturated porous media: Wetting film versus disconnectedness of the conducting
601 phase. Phys. Rev. E. 79,doi:10.1103/PhysRevE.79.031127.

602 Hignett, C., and S.R. Evett. 2002. Neutron thermalization. In: J.H. Dane and G.C. Topp, editors,
603 Methods of soil analysis. Part 4 B. Physical methods. SSSA Book Series No. 5, Soil Sci. Soc.
604 Amer., Madison, WI. p. 501–521.

605 Hubbard, S.S. and N. Linde, 2011. Hydrogeophysics. In: P. Wilderer, editor, Treatise on water
606 science. Vol. 1. Academic Press, Oxford, p. 401–434.

607 Hubbard, S.S., J.E. Peterson, E.L. Majer, P.T. Zawislanski, J. Roberts, K.H. Williams, and
608 F. Wobber. 1997. Estimation of permeable pathways and water content using tomographic radar
609 data. The Leading Edge of Exploration 16(11):1623–1628.

610 Huisman, J.A., C. Sperl, W. Bouten, and J.M. Verstraten. 2001. Soil water content measurements
611 at different scales: accuracy of time domain reflectometry and ground-penetrating radar.
612 J. Hydrol. 245:48–58.

613 Jackson, M.J., and D.R. Tweeton. 1994. MIGRATOM - Geophysical tomography using
614 wavefront migration and fuzzy constraints. Bureau of Mines Report of Investigations 9497,
615 U.S. Department of the Interior, Washington, D.C..

616 Johnson, T.C., R.J. Versteeg, A. Ward, F.D. Day-Lewis, and A. Revil. 2010. Improved
617 hydrogeophysical characterization and monitoring through parallel modeling and inversion of
618 time-domain resistivity and induced polarization data. Geophysics. 75(4):WA27–WA41.

619 Laloy, E., N. Linde, and J.A. Vrugt. 2012. Mass conservative three-dimensional water tracer
620 distribution from Markov chain Monte Carlo inversion of time-lapse ground-penetrating radar
621 data. Water Resour. Res. 48:W07510, doi:10.1029/2011WR011238.

622 Ledieu, J., P. De Ridder, P. De Clerck, and S. Dautrebande. 1986. A method of measuring soil
623 moisture by time-domain reflectometry. J. Hydrol. 88:319–328.

624 Lesmes, D., and S. Friedman. 2005. Electrical and hydrological properties. In: Y. Rubin and
625 S. Hubbard, editors, Hydrogeophysics. Springer, The Netherlands. p. 87–128.

626 Oostrom, M., T.W. Wietsma, J.H. Dane, M.J. Truex, and A.L. Ward. 2009. Desiccation of
627 unsaturated porous media: Intermediate-scale experiments and numerical simulation. Vadose
628 Zone J. 8:643–650.

629 Oostrom, M., T.W. Wietsma, C.E. Strickland, V.L. Freedman, and M.J. Truex. 2011. Sensor and
630 numerical simulator evaluation for porous medium desiccation and rewetting at the intermediate
631 laboratory scale. Vadose Zone J. 11(1), doi: 10.2136/vzj2011.0089.

632 Oostrom, M., V.L. Freedman, T.W. Wietsma, and M.J. Truex. 2012a. Effects of porous
633 medium heterogeneity on vadose zone desiccation: Intermediate-scale laboratory experiments
634 and simulations. *Vadose Zone J.*, doi:10.2136/vzj2011.0168.

635 Oostrom, M., T.W. Wietsma, C.E. Strickland, V.L. Freedman, and M.J. Truex. 2012b.
636 Instrument testing during desiccation and rewetting at the intermediate laboratory scale. *Vadose*
637 *Zone J.*, doi:10.2136/vzj2011.0089.

638 Or, D., and J.M. Wraith. 1999. Temperature effects on soil bulk dielectric permittivity measured
639 by time domain reflectometry: A physical model. Water Resour. Res. 35(2):371–383,
640 doi: 10.1029/1998WR900008.

641 Peterson, J. 2001. Pre-inversion Corrections and Analysis of Radar Tomographic Data.
642 J. Environ. Eng. Geophysics 6(1), doi: 10.4133/JEEG6.1.1

643 Revil, M., M. Karaoulis, T. Johnson, and A. Kemna. 2012. Some low-frequency electrical
644 methods for subsurface characterization. Hydrogeology Journal 15(16), doi: 10.1007/s10040-
645 011-0819-x.

646 Rubin, Y., and S. Hubbard (editors). 2005. Hydrogeophysics, Water and Science Technology
647 Library. Vol 50. Springer, The Netherlands.

648 Ruijun, M., A. McBratney, B. Whelan, B. Minasny, and M. Short. 2011. Comparing temperature
649 correction models for soil electrical conductivity measurement. Prec. Ag. 12:55–66,
650 doi: 10.1007/s11119-009-9156-7.

651 Serne RJ, AL Ward, W Um, BN Bjornstad, DF Rucker, DC Lanigan, and MW Benecke. 2009.
652 Electrical resistivity correlation to vadose zone sediment and pore-water composition for the BC
653 cribs and trenches area. PNNL-17821, Pacific Northwest National Laboratory, Richland,
654 Washington.

655 Slater, L.D., and D.P. Lesmes. 2002. Electrical-hydraulic relationships observed for
656 unconsolidated sediments. Water Resour. Res. 38:1213–1225.

657 Topp, G.C., and P.A. (Ty) Ferré. 2002. Water content. In: J.H. Dane and G.C. Topp, editors,
658 Methods of soil analysis. Part 4. Physical methods. SSSA Book Series No. 5, Soil Sci. Soc.
659 Amer., Madison, WI.

660 Topp, G.C., and W.D. Reynolds. 1998. Time domain reflectometry: a seminal technique for
661 measuring mass and energy in soil. Soil and Tillage Res. 47:125–132.

662 Topp, G.C., J.L. Davis, and A.P. Annan, 1980. Electromagnetic determination of soil water
663 content: Measurements in coaxial transmission lines. Water Resour. Res. 16(3):574–582,
664 doi: 10.1029/WR016i003p00574.

665 Truex, M.J., M. Oostrom, V.L. Freedman, C.E. Strickland, and A.L. Ward. 2011. Laboratory and
666 modeling evaluations in support of field testing for desiccation at the Hanford Site.
667 PNNL-20146, Pacific Northwest National Laboratory, Richland, WA.

668 Truex, M.J., M. Oostrom, C.E. Strickland, G.B. Chronister, M.W. Benecke, and C.D. Johnson.
669 2012a. Field-scale assessment of desiccation implementation for deep vadose zone
670 contaminants. Vadose Zone J. doi: 10.2136/vzj2011.0144.

671 Truex, M.J., M. Oostrom, C.E. Strickland, T.C. Johnson, V.L. Freedman, C.D. Johnson,
672 W.J. Greenwood, A.L. Ward, R.E. Clayton, M.J. Lindberg, J.E. Peterson, S.S. Hubbard,
673 G.B. Chronister, and M.W. Benecke. 2012b. Deep vadose zone treatability test for the Hanford
674 Central Plateau: Soil desiccation pilot test results. PNNL-21369, Pacific Northwest National
675 Laboratory, Richland, WA.

676 Um W, RJ Serne, MJ Truex, AL Ward, MM Valenta, CF Brown, C Iovin, KN Geiszler, IV
677 Kutnyakov, ET Clayton, H-S Chang, SR Baum, and DM Smith. 2009. Characterization of

678 sediments from the soil desiccation pilot test (SDPT) site in the BC cribs and trenches area.
679 PNNL-18800, Pacific Northwest National Laboratory, Richland, Washington.

680 Van Overmeeren, R., S. Sariowan, and J. Geherls. 1997. Ground penetrating radar for
681 determining volumetric soil water content: Results of comparative measurements at two test
682 sites. J. Hydrol. 197:316–338.

683 Vereecken, H., A. Binley, G. Gassiani, A. Revil, and K. Titov. 2006. Applied Hydrogeophysics.
684 NATO Science Series, Earth and Environmental Science Vol. 71, Springer, The Netherlands.

685 Ward A.L., M. Oostrom, and D.H. Bacon. 2008. Experimental and numerical investigations of
686 soil desiccation for vadose zone remediation: Report for fiscal year 2007. PNNL-17274, Pacific
687 Northwest National Laboratory, Richland, WA.

688 Waxman, M.H., and L.J.M. Smits. 1968. Electrical conduction in oil-bearing sands. SPE Journal
689 8:107–122.

690 Waxman, M.H., and E.C. Thomas. 1974. Electrical conductivities in shaly sands: Part 1—The
691 relation between hydrocarbon saturation and resistivity index; Part 2—The temperature
692 coefficient of electrical conductivity. Journal of Petroleum Technology. 26:213–225.

693 White, I., and S. J. Zegelin. 1995. Electric and dielectric methods for monitoring soil-water
694 content. In: L.G. Wilson, L.G. Everett, and S. Cullen, editors, Handbook of Vadose Zone
695 Characterization and Monitoring, A.F. Lewis, New York.

696

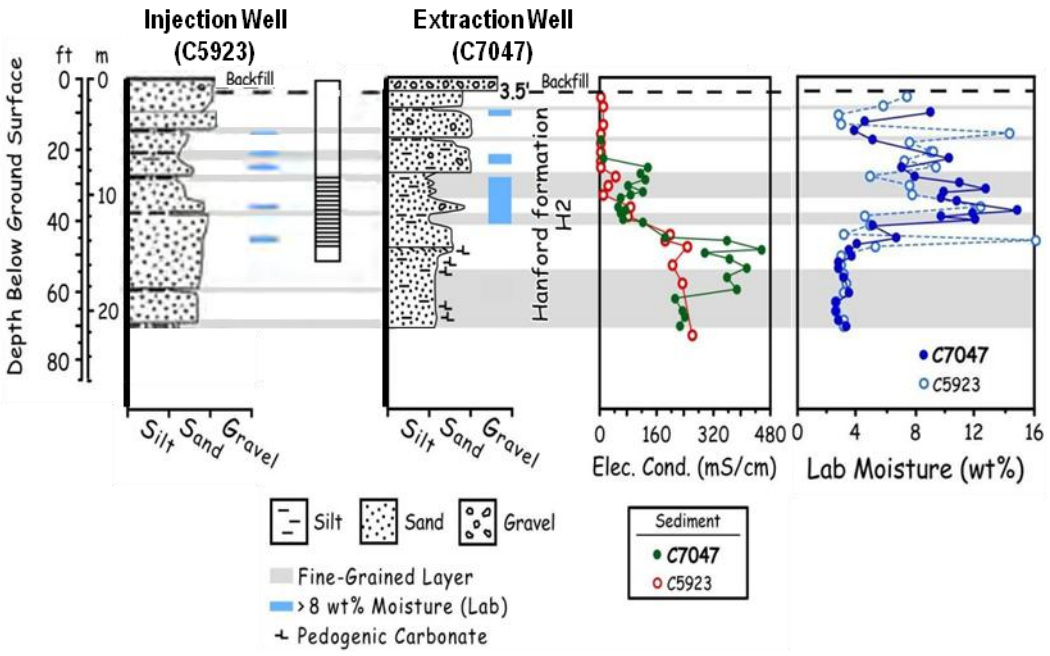

697

698 Figure 1. Injection and extraction well borehole laboratory moisture content, extracted pore water
699 electrical conductivity, and well screened interval (after DOE 2010; Serne et al. 2009; Um et al. 2009).
700 Electrical conductivity was measured on pore water extracted from sediment samples.

701

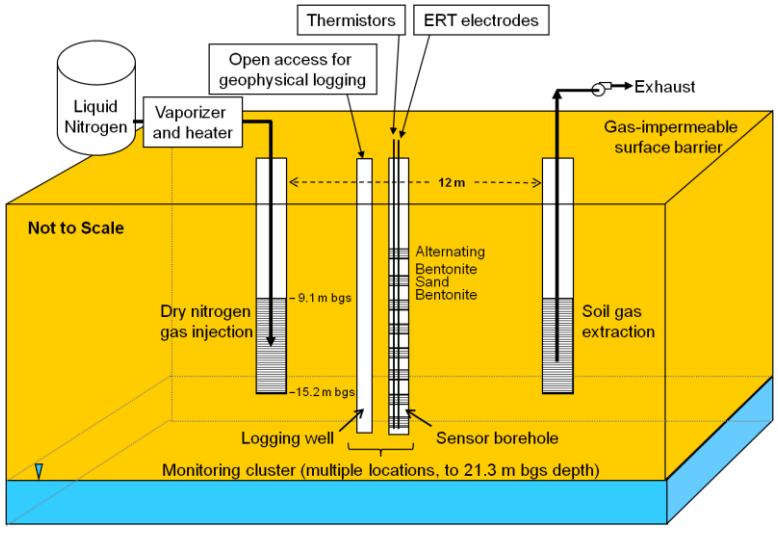

702

703 Figure 2. Basic components of the desiccation field test system.

704

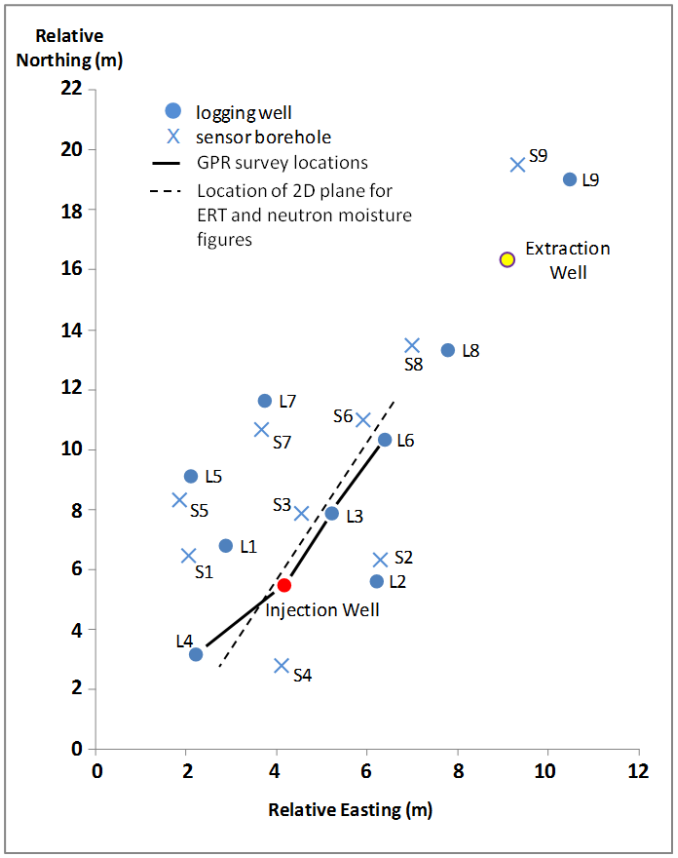

Figure 3. Location of test site wells, where boreholes with an "S" designation contained in situ thermistors and ERT electrodes and wells with an "L" designation were cased wells for neutron logging and GPR access.

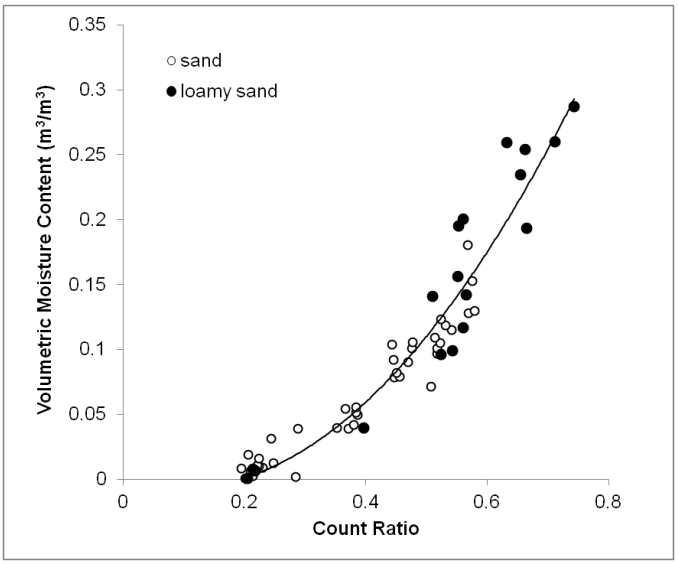

710

711 Figure 4. Calibration relation for neutron moisture probe count ratio data and corresponding laboratory-
712 measured volumetric moisture content (after Truex et al. 2012a).

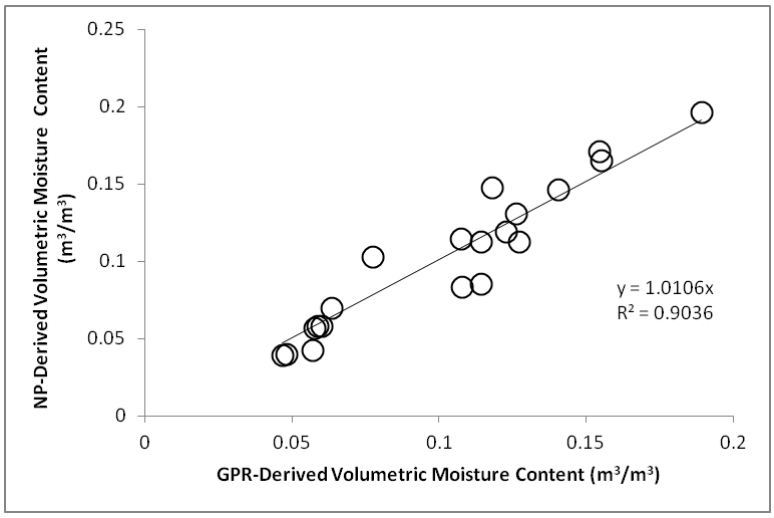

713

714 Figure 5. Comparison of volumetric moisture content derived from GPR and neutron moisture logging
715 (NP) for location L4 at depths less than 10 m prior to desiccation.

716

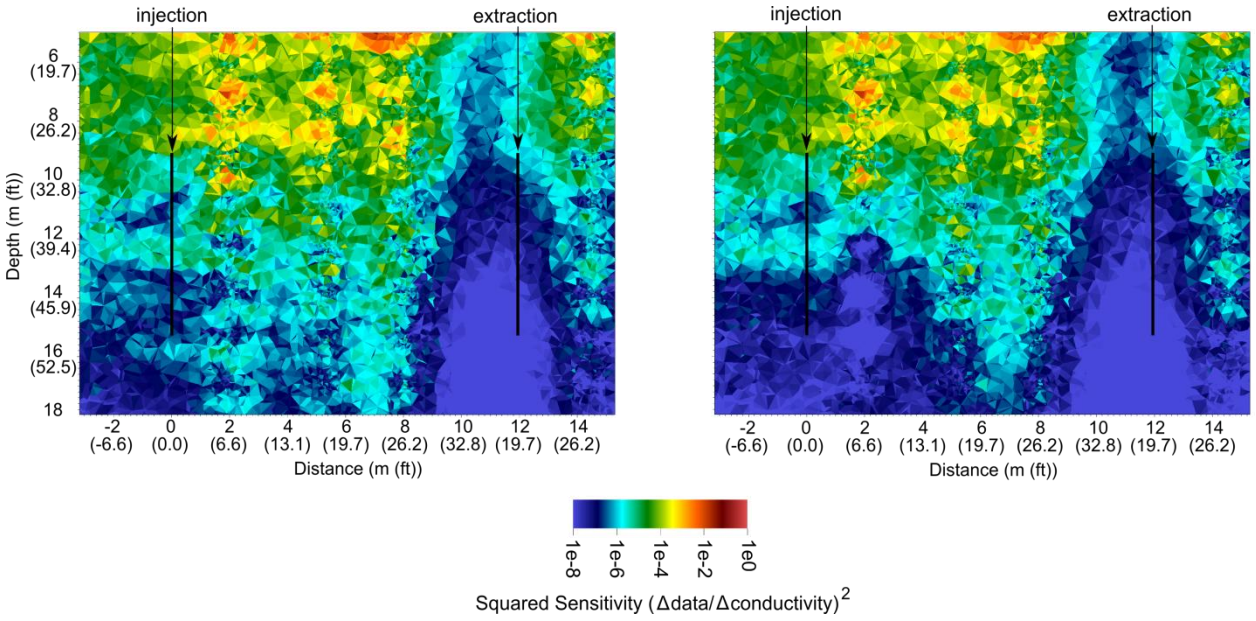

717

718 Figure 6. ERT data sensitivity distribution for given data available before desiccation (left) and after
719 desiccation (right). The loss in sensitivity surrounding the injection well from approximately 14 m to 16
720 m depth is caused by a loss of electrode coupling within the desiccation zone. The images are shown in
721 true dimension (i.e. no smoothing between tetrahedral elements is applied).

722

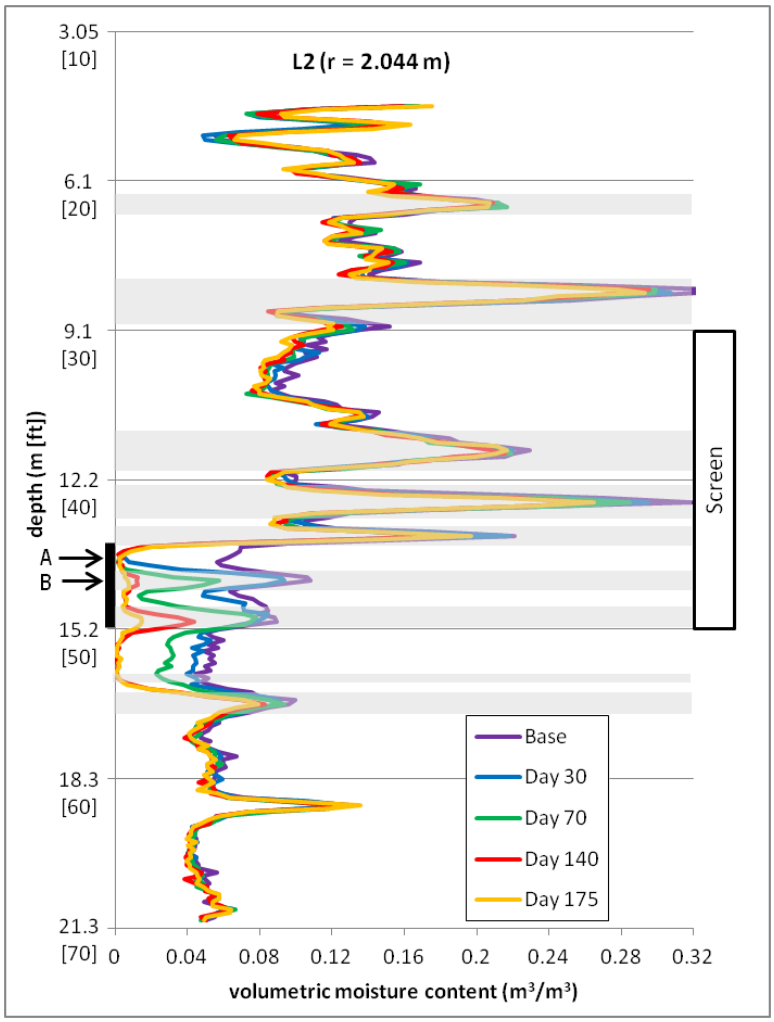

723

724 Figure 7. Neutron moisture data at location L2 in days from start of active desiccation. Base data are pre-
725 desiccation. Day 175 represents the end of active desiccation. Zones of loamy sand (gray) and sand (no
726 shading) textures are shown for the depth interval 6 to 18 m bgs where samples were evaluated from a
727 post-desiccation borehole located 0.9 m away (after Truex et al. 2012a).

728

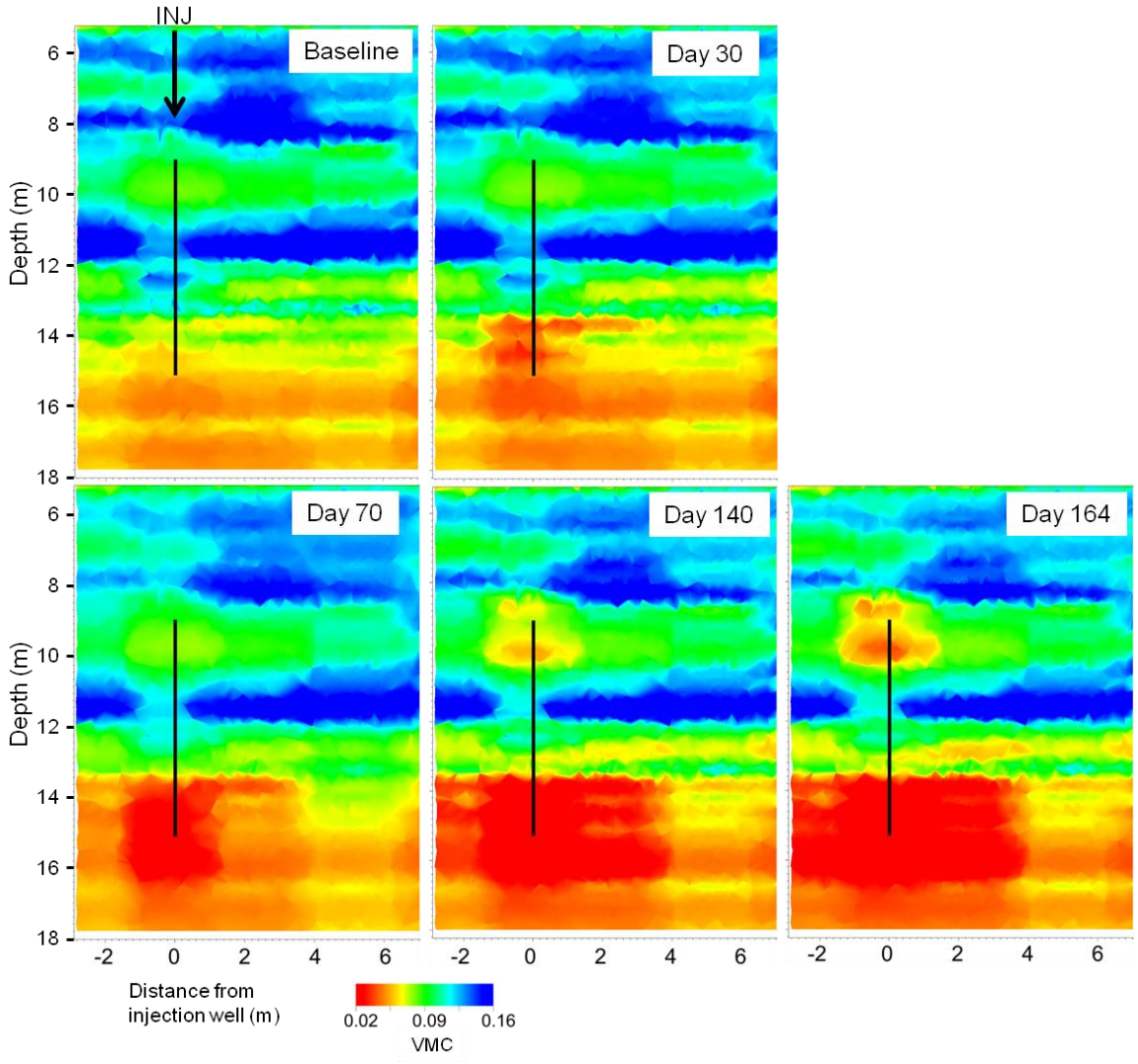

729

730 Figure 8. Interpolation of volumetric moisture content (VMC) from neutron moisture logging data along
731 the axis between the injection and extraction wells. Neutron moisture data from are from logging at
732 locations L1-L7 (Figure 3). The black line indicates the screened section of the injection well.

733

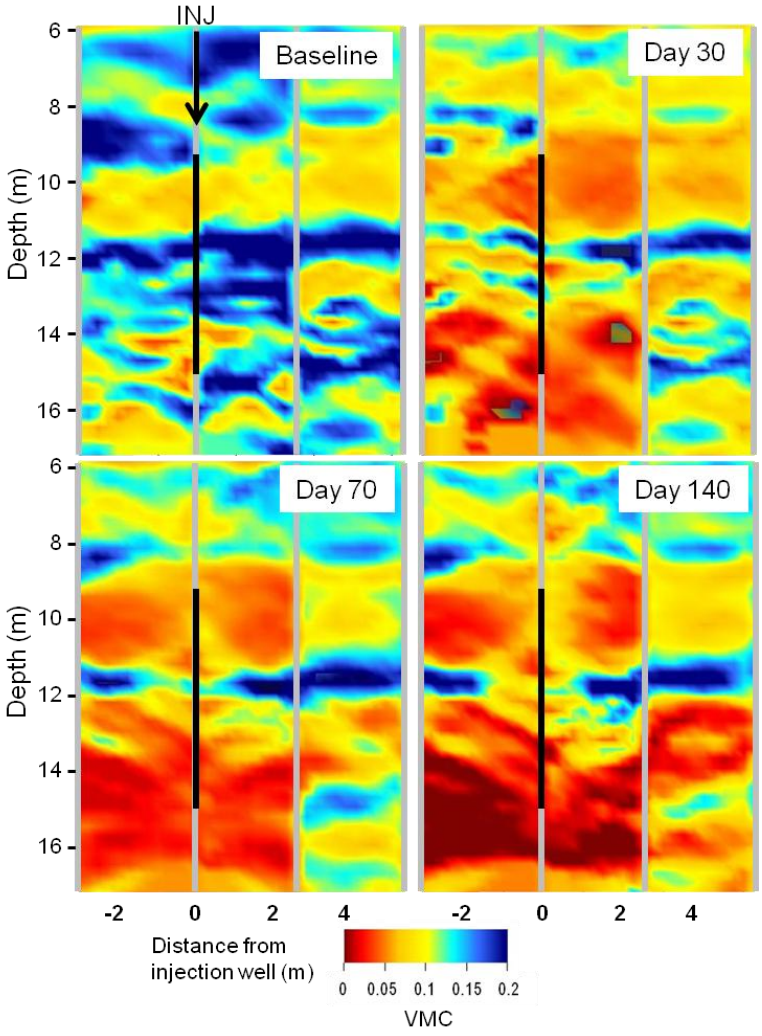

734

735 Figure 9. 2-D interpretation of volumetric moisture content (VMC) from cross-hole GPR data. See text
736 and Figures 10 and 11 for interpretation of moisture content in relation to the low-loss assumption. The
737 black line indicates the screened section of the injection well.

738

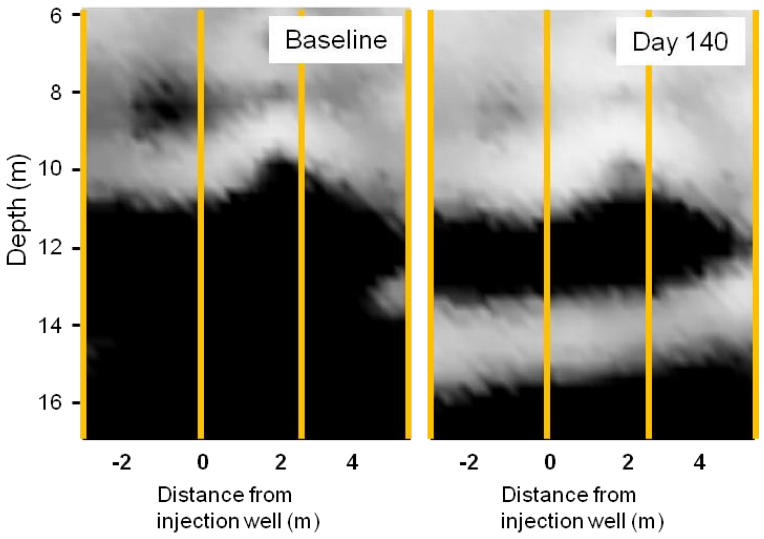

739

740 Figure 10. Electrical conductivity distribution showing regions where the low-loss conditions can be
741 assumed (light regions). Black regions show where the electrical conductivity is greater than 0.05 S/m
742 and the low-loss assumption cannot be applied.

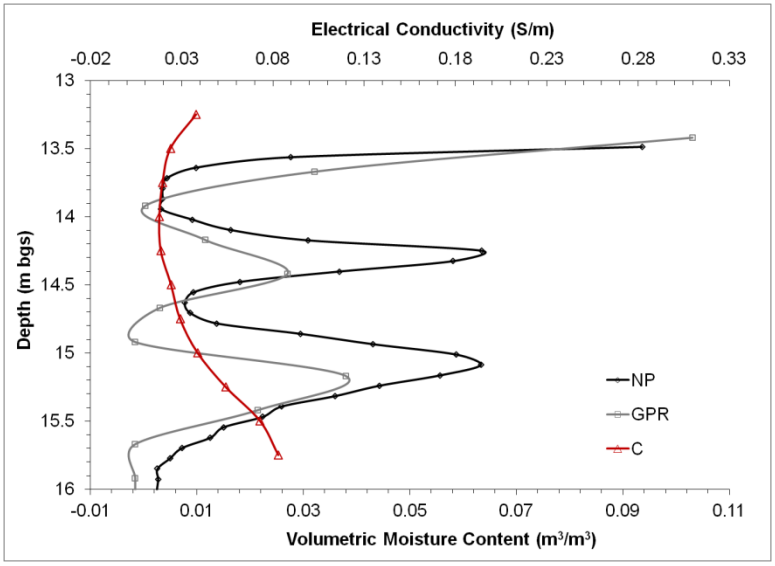

743

744 Figure 11. Comparison of post-desiccation volumetric moisture content from GPR and neutron moisture
745 logging (NP) for location L3 within a depth interval where electrical conductivity (C) has been decreased
746 by desiccation (Figure 10).

747

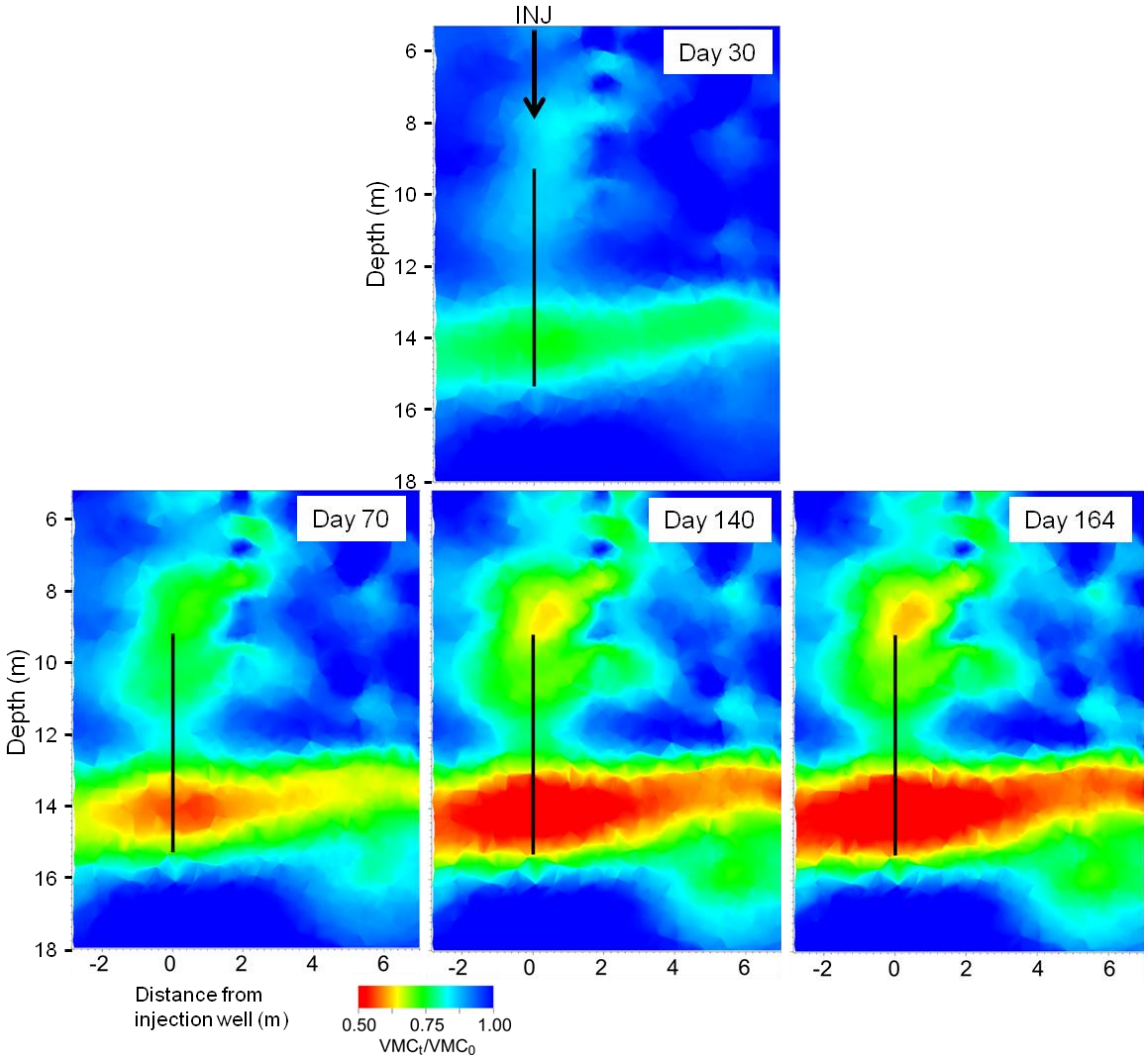

748

749 Figure 12. Ratio of volumetric moisture content (VMC_t) to pre-desiccation volumetric moisture content
750 (VMC_0) over time along the axis between the injection and extraction wells from cross-hole ERT. ERT
751 data are from sensors at locations S1-S7 (Figure 3). The black line indicates the screened section of the
752 injection well.

753

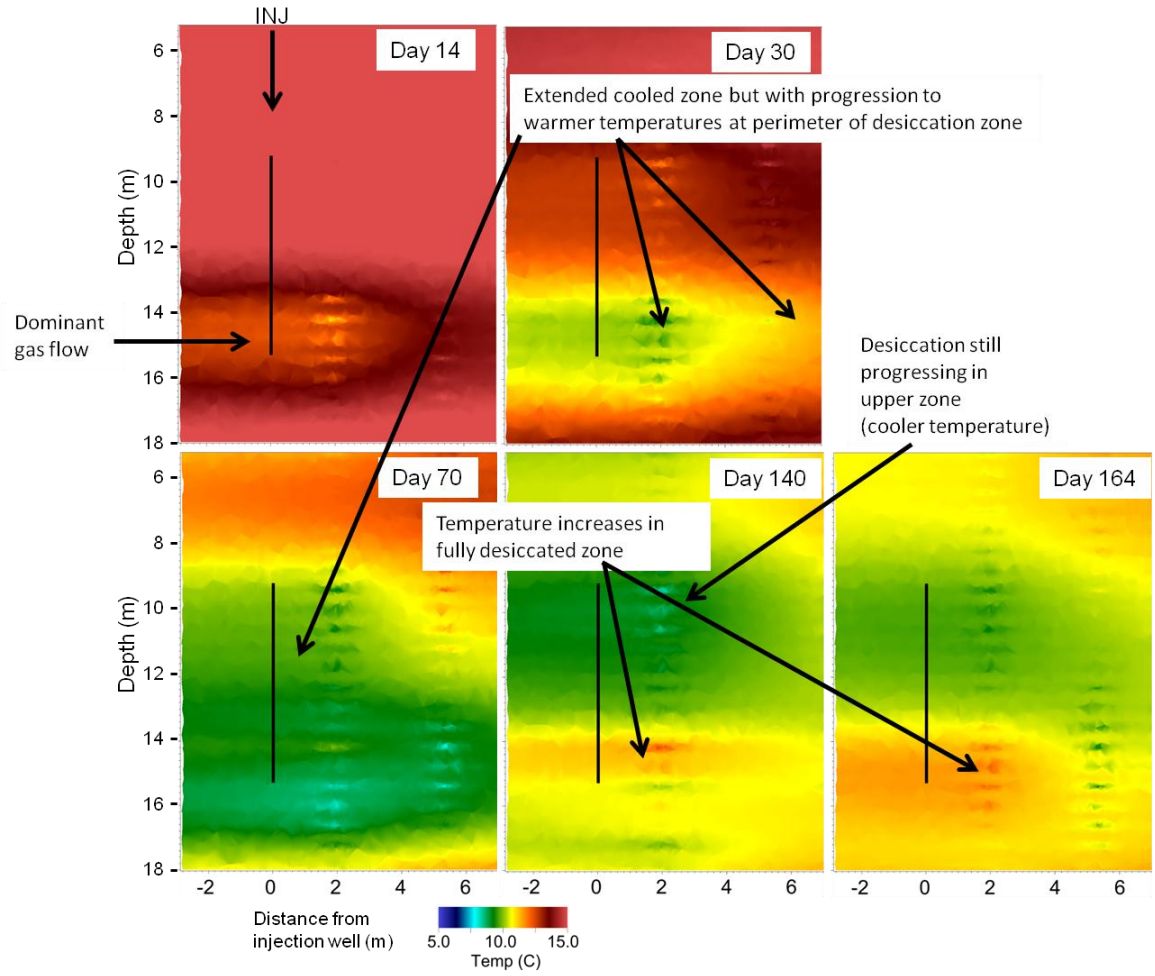

754

755 Figure 13. Interpolated temperature response along the axis between the injection and extraction wells,
756 indirectly showing desiccation through the evaporative cooling effect. Temperatures drop while a zone is
757 being desiccated. Once a zone is fully desiccated, there is no more evaporative cooling and temperature
758 rises toward the inlet temperature. Data from sensors at locations S1-S7 (Figure 3).

759